

The Photospheric Poynting Flux and Coronal Heating

B. T. WELSCH

Space Sciences Laboratory, UC, Berkeley

welsch@ssl.berkeley.edu

(Received 2014 February 28; accepted 2014 December 2)

Abstract

Some models of coronal heating suppose that convective motions at the photosphere shuffle the footpoints of coronal magnetic fields and thereby inject sufficient magnetic energy upward to account for observed coronal and chromospheric energy losses in active regions. Using high-resolution observations of plage magnetic fields made with the Solar Optical Telescope aboard the *Hinode* satellite, we investigate this idea by estimating the upward transport of magnetic energy — the vertical Poynting flux, S_z — across the photosphere in a plage region. To do so, we combine: (i) estimates of photospheric horizontal velocities, \mathbf{v}_h , determined by local correlation tracking applied to a sequence of line-of-sight magnetic field maps from the Narrowband Filter Imager, with (ii) a vector magnetic field measurement from the SpectroPolarimeter. Plage fields are ideal observational targets for estimating energy injection by convection, because they are: (i) strong enough to be measured with relatively small uncertainties; (ii) not so strong that convection is heavily suppressed (as within umbrae); and (iii) unipolar, so S_z in plage is not influenced by mixed-polarity processes (e.g., flux emergence) unrelated to heating in stable, active-region fields. In this plage region, we found that the average S_z varied in space, but was positive (upward) and sufficient to explain coronal heating, with values near $(5 \pm 1) \times 10^7$ erg cm⁻² s⁻¹. We find the energy input per unit magnetic flux to be on the order of 10^5 erg s⁻¹ Mx⁻¹. A comparison of intensity in a Ca II image co-registered with one plage magnetogram shows stronger spatial correlations with both total field strength and unsigned vertical field, $|B_z|$, than either S_z or horizontal flux density, B_h . The observed Ca II brightness enhancement, however, probably contains a strong contribution from a near-photosphere hot-wall effect, which is unrelated to heating in the solar atmosphere.

Key words: Magnetic Fields — Sun:photosphere — Sun:corona

1. Introduction

How is the solar corona heated to temperatures of ~ 1 MK, when the lower layers of the solar atmosphere are $\sim 10^4$ K or less? Evidently, the energy needed to heat the Sun's atmosphere must cross the photosphere in some organized form before being converted into heat (disorganized, “thermalized” energy) in the chromosphere and corona. Because the magnetic fields that permeate the corona are all anchored at the photosphere, they are natural candidates for energetic coupling between the solar interior and corona. In the interior, motions in the Sun's gas are driven by convection, and some fraction of the kinetic energy in turbulent convective motions is thought to be converted into energy stored in electric currents flowing in coronal magnetic fields that is then dissipated as heat. These induced currents might be characterized as either steady or rapidly varying (e.g., wave-driven) relative to the timescales of the atmospheric response, and the dissipation of each has been referred to as “DC” (direct-current) or “AC” (alternating-current) heating, respectively (e.g., Klimchuk 2006).

To be a viable coronal heating mechanism, the input energy must be commensurate with observed energy losses in active region (AR) fields, estimated by Withbroe & Noyes (1977) to be $\sim 1 \times 10^7$ erg cm $^{-2}$ s $^{-1}$ for the corona and $\sim 2 \times 10^7$ erg cm $^{-2}$ s $^{-1}$ for the chromosphere. Waves were once thought to be primarily responsible for coronal and chromospheric heating (see, e.g., Withbroe and Noyes 1977). While waves (e.g., Tomczyk et al. 2007) and wave dissipation (e.g., Hahn et al. 2012) have been reported in the corona, currently available observations have not demonstrated that they supply sufficient energy to heat the active-region chromosphere, transition region, and corona. In contrast to models invoking dissipation of waves, other models posit that convective motions induce relatively long-lived, DC currents that are episodically dissipated to heat the chromosphere and corona. We explore the latter hypothesis here.

There is a long history of modeling this convection-driven coronal energy input. Parker (1983a, 1983b) proposed that convection braids and twists the photospheric footpoints of coronal magnetic fields, and thereby injects energy into the corona. This energy is stored in current sheets, and is transiently dissipated in small bursts referred to as nanoflares (Parker 1988), with typical energies of $\sim 10^{24}$ erg, about 10^{-9} of the energies in very large flares. Galsgaard & Nordlund (1996) modeled an idealization of this process by imposing shearing flows on the upper and lower boundaries of an initially uniform field in an MHD simulation, and found sufficient power to heat the corona. Gudiksen & Nordlund (2002) imposed a more complex flow field, meant to mimic convective motions, on an MHD model of the coronal field and also found sufficient power, as well as morphology consistent with aspects of coronal observations. In the framework of reduced MHD, Rappazzo et al. (2008), also found sufficient power, even though fields in their model were only weakly braided. More recently, Bingert & Peter (2011) also modeled this process in MHD with a detailed treatment of the energy equation and found heating that is transient in time and space, and concentrated in and near the modeled transition

region.

One promising observational approach to constraining models of coronal heating is to analyze time evolution of magnetic fields at the photosphere, where the magnetic field is precisely and routinely measured. Clear evidence of braiding or twisting motions would support the mechanism proposed by Parker. Schrijver et al. (1998) proposed that continuous emergence and cancellation of small-scale fields in the quiet Sun’s “magnetic carpet” leads to reconnection and heating, but Close et al. (2004) used sequential potential models of quiet-Sun fields to argue that emergence and cancellation are not required: just reconnection between existing flux systems, as their photospheric footpoints move, should be sufficient. Meyer et al. (2013) recently directly incorporated magnetogram sequences into the lower boundary of a magnetofrictional model of quiet-sun coronal field evolution, to investigate the dissipation of magnetic energy within the simulation. Aspects of energy dissipation in their model were qualitatively consistent with solar observations, although their total upward energy flux was smaller than the observationally estimated energy demand for the quiet-sun atmosphere.

Yeates et al. (2014) recently investigated analytic expressions for lower bounds on the upward-directed Poynting flux of magnetic energy in a region of plage fields in NOAA AR 10930, based upon observed photospheric magnetic and velocity fields. The flows they analyzed were estimated by Welsch et al. (2012), who applied Fourier Local Correlation Tracking (FLCT; Fisher and Welsch 2008) to a sequence of line-of-sight magnetograms (magnetic field maps) of this active region. These magnetograms were observed with the Narrowband Filter Imager (NFI) instrument on the Solar Optical Telescope (SOT) (Tsuneta et al. 2008; Suematsu et al. 2008; Ichimoto et al. 2008; Shimizu et al. 2008) aboard the *Hinode* satellite (Kosugi et al. 2007), with a cadence $\simeq 120$ s, over about 13 hours on 2006 December 12 – 13.

Yeates et al. (2014) compared their lower bounds on the Poynting flux with a direct estimate of the Poynting flux, obtained with a procedure that we explain in detail here. First, they assumed that the photospheric magnetic field, \mathbf{B} , is frozen to the plasma — a valid assumption in quite general circumstances (see, e.g., Parker 1984). Then the photospheric electric field, \mathbf{E} , is ideal, and equal to $-(\mathbf{v} \times \mathbf{B})/c$, where \mathbf{v} is the photospheric velocity. Then the (vector) Poynting flux of magnetic energy, \mathbf{S} , can be expressed in terms of \mathbf{v} and \mathbf{B} as

$$\mathbf{S} = \mathbf{B} \times (\mathbf{v} \times \mathbf{B})/4\pi . \tag{1}$$

Approximating the photospheric surface as locally planar, we adopt Cartesian geometry, and use z and h to refer to vertical and horizontal directions, respectively. Then the vertical component of the Poynting flux is

$$S_z = [v_z B_h^2 - (\mathbf{v}_h \cdot \mathbf{B}_h) B_z]/4\pi . \tag{2}$$

This expression for total Poynting flux has been conceptually divided into an “emergence” term, which contains v_z , and a “shear” term, which contains \mathbf{v}_h (Liu & Schuck 2012; Parnell & De Moortel 2012).

We digress for a moment to note that a positive (upward) value for the shearing term also implies the emergence of magnetized plasma across the photosphere. A clear example of this is the special case in which v_z is zero (so the emergence term vanishes), and the shearing term is positive. Then both B_z and \mathbf{B}_h must be nonzero, implying \mathbf{B} is tilted; and \mathbf{v}_h must have a nonzero projection onto \mathbf{B}_h . We define the component of \mathbf{v}_h along the horizontal field \mathbf{B}_h to be \mathbf{v}_{Bh} , and then further decompose \mathbf{v}_{Bh} into a component parallel to the total field \mathbf{B} , which we label $v_{Bh,\parallel}$, and a component perpendicular to \mathbf{B} , which we label $v_{Bh,\perp}$. Since \mathbf{B} is tilted, $v_{Bh,\perp}$ must also be; and it must be tilted upward when the shearing term is positive. This upward tilt for $v_{Bh,\perp}$ implies that this component of the flow advects the tilted magnetic flux upward. The parallel flow $v_{Bh,\parallel}$ neither advects magnetic field or produces a Poynting flux. The counter-intuitive result that a horizontal velocity can produce upward transport of magnetic fields arises because the total velocity included a component of the velocity parallel to \mathbf{B} , which is irrelevant for the Poynting flux. (In the special case that the parallel velocity is zero, then equation [1] reduces to $\mathbf{S} = B^2\mathbf{v}/4\pi$, and equation [1] becomes $S_z = B^2v_z/4\pi$.)

Since Yeates et al. (2014) were primarily focused on heating in plage — regions of nearly-vertical field when new flux is not emerging — the shearing term should dominate, meaning

$$S_z^{\text{plage}} \simeq -(\mathbf{v}_h \cdot \mathbf{B}_h)B_z/4\pi . \quad (3)$$

Yeates et al. (2014) treated the flows estimated by FLCT as horizontal velocities. We note that there is some controversy about how to interpret of velocities determined by correlation tracking and other “optical flow” (Schuck 2006) methods. Démoulin & Berger (2003) suggested that the apparently horizontal flows estimated by LCT are a linear combination of the horizontal velocity with the vertical velocity, with weighting determined by the ratio of horizontal to vertical magnetic field. To test the accuracy of velocities reconstructed from magnetogram sequences, Welsch et al. (2007) compared flows estimated by several methods, including LCT, using synthetic magnetograms extracted from MHD simulations of an emerging magnetic flux tube in the solar interior in which the actual velocities were known. Using the same test data, Schuck (2008) subsequently argued that optical flow methods, such as LCT, essentially estimate the horizontal velocity, \mathbf{v}_h , although their estimates can be affected by vertical flows.

The NFI magnetograms only provide estimates of the line-of-sight (LOS) field, B_{LOS} , but the expressions for the Poynting flux given above all require knowledge of the vector magnetic field, \mathbf{B} . Accordingly, Yeates et al. (2014) co-registered the (12 Mm \times 12 Mm) region of the NFI field of view (FOV) that they studied with the corresponding sub-region of a vector magnetogram observed by SOT’s SpectroPolarimeter (SP; Lites et al. 2013). A reprojected vector magnetogram based upon these observations was prepared by Schrijver et al. (2008) and is available online. The co-alignment procedure followed the approach used by Welsch et al. (2012), described in their Appendix.

By combining \mathbf{v}_h estimated with FLCT with \mathbf{B} from the SP magnetogram, Yeates et al. (2014) estimated the average Poynting flux to be 1.7×10^7 erg cm⁻² s⁻¹. This energy flux is less than the combined energy demand for the chromosphere and corona in active regions estimated by Withbroe & Noyes (1977). As discussed in greater detail below, however, this estimate did not account for the observationally estimated magnetic filling factors that had been applied to each magnetic field component in the vector magnetogram used by Schrijver et al. (2008). Insufficient Poynting flux would indicate that processes on spatial or temporal scales that are unresolved in these photospheric observations (e.g., waves or smaller-scale footpoint shuffling) play a significant role in heating.

Despite the central role of the Poynting flux in theories of coronal heating, very few observational estimates of Poynting flux in the context of coronal heating have been published. Tan et al. (2007) investigated a “proxy Poynting flux,” $|\mathbf{v}_h|B_{\text{LOS}}^2$ in more than 160 active regions, determined by applying LCT to LOS magnetograms, and found values in the range $10^{6.7} - 10^{7.6}$ erg cm⁻² s⁻¹. They used the LOS fields alone because sequences of vector magnetic field measurements were quite rare. More recently, Kano et al. (2014) estimated the work done by flows on the magnetic field, by parametrizing the expected deformation of coronal loop structure by surface flows. The expression they derive is inversely proportional to coronal loop length $L \sim 100$ Mm, and for LCT flows with typical magnitudes of 0.5 km s⁻¹, they estimate a Poynting flux of 2×10^6 erg s⁻¹ cm². They also found typical flow speeds were lower in regions with higher magnetic filling factors. This is roughly an order of magnitude lower than the value of 1.7×10^7 erg s⁻¹ cm² reported by Yeates et al. (2014). Given this considerable variation in published Poynting flux estimates, further investigation of Poynting fluxes is warranted.

Here, we report additional estimates of the Poynting flux from plage magnetic fields in the same active region studied by Yeates et al. (2014). Our primary aim is to investigate the properties of photospheric Poynting flux in greater detail than was done previously, including its dependence on photospheric magnetic field structure. The remainder of this paper is organized as follows. In the next section, we briefly describe the magnetic field data and tracking methods we used to estimate \mathbf{v}_h . In Section 3, we first present our estimates of the Poynting flux in another small region of plage in AR 10930, then analyze the Poynting flux’s correlations with magnetic structure in the region. The region of the NFI FOV that we analyze here was also observed in Ca II by SOT’s Broadband Filter Imager (BFI; Tsuneta et al. 2008), and in §3.4 we compare this chromospheric emission with the spatial distributions of Poynting flux and magnetic field components. Finally, we conclude with a brief discussion of our results in Section 4.

2. Data & Methods

2.1. NFI Magnetograms

Many aspects of the NFI magnetograms that we track to estimate \mathbf{v}_h are described by Welsch et al. (2012). These Fe I 6302 Å (shuttered) magnetograms of AR 10930 have 0."16 pixels, and were created from the Stokes V/I ratio in Level 0 data. The data were recorded between 12-Dec-2006 at 14:00 and 13-Dec-2006 at 02:58, with a cadence of 121.4 ± 1.2 s, except for three gaps of 10 minutes and two relatively small time steps of 26 s each. The USAF/NOAA Solar Region Summary issued at 24:00 UT on 12-Dec-2006 listed AR 10930 at S06W21, meaning it was relatively near disk center during the interval we study. Since the diffraction limit of SOT is near 0."32, we rebinned the NFI magnetograms (2×2). During this era of the *Hinode* mission, a bubble present within the NFI instrument degraded image quality in the upper part of the NFI field of view; we ignore pixels from this region in our analyses.

We converted the measured Stokes I and V signals into pixel-averaged flux densities, which we denote B_{NFI} , using the approximate calibration employed by Isobe et al. (2007). While the linear scaling in this approach breaks down in umbrae, it should not be problematic for plage regions. Note that we use evolution in image structure in the NFI magnetograms to derive velocities, but do not use the estimated flux densities directly in any calculations; for correlation tracking, what matters is that the images capture the *spatial structure* of magnetic fields at each time in the sequence. Welsch et al. (2012) estimated the NFI noise level following Hagenaar et al. (1999), by fitting the core of the distribution of flux densities (± 10 Mx cm $^{-2}$) in each frame with a Gaussian. Based upon these fits, they adopted a uniform uncertainty estimate of ± 15 Mx cm $^{-2}$ for B_{NFI} over the 13-hour run.

Prior to tracking these magnetograms, Welsch et al. (2012) co-aligned them in time to remove spacecraft jitter and jumps from pointing changes. Spectral analysis showed some power at the orbital frequency, but no clear evidence of helioseismic p-mode leakage into the estimated magnetic flux densities.

2.2. SP Vector Magnetograms

As mentioned above, Schrijver et al. (2008) used SP data to estimate the vector magnetic field in AR 10930, and one of the two vector magnetograms they analyzed falls within our tracking interval. The full SP scan ran from 20:30 - 21:33, with $\sim 0."$ 3 pixels. From these observations, LOS and transverse magnetic field strengths, azimuth and fill fraction were determined at each SP slit position, as described by Schrijver et al. (2008). The data were then interpolated onto a uniform grid in the plane-of-the-sky, with 0."32 square pixels, multiplied by the fill fraction, and annealed to set the ambiguity resolution. Notably, in pixels with weak total polarization, the fill-fraction was set to 1.0. We refer to this plane-of-sky (POS) SP magnetogram as the POSSP magnetogram. To produce the vector magnetogram used by both

Schrijver et al. (2008) and Yeates et al. (2014), the resulting fields were then reprojected to represent the magnetic field on a Cartesian plane and mapped onto a grid with a pixel scale of approximately $0.''63$ per pixel. (This was done to reduce the array size for computational expediency in extrapolating coronal fields.) We refer to this reduced-resolution SP magnetogram as the RRSP magnetogram. (The RRSP magnetogram produced by Schrijver et al. (2008) is online, in FITS format, at <http://www.lmsal.com/~schryver/NLFFF/>; file contents are described in the FITS header comment field.)

When fill fractions are estimated in the process of inverting spectropolarimetric data to infer the magnetic field, the form of equation (3) should be modified (Katsukawa & Tsuneta 2005; Kano et al. 2014) to properly account for the filling factor, $f(x, y)$,

$$S_z^{\text{plage}} \simeq -f(\mathbf{v}_h \cdot \mathbf{B}_h)B_z/4\pi . \quad (4)$$

That is, the product of intrinsic field strengths should be weighted by one factor of f . Since each magnetic field component, B_i , in both the POSSP and RRSP magnetograms was already weighted by f , using these values in equation (4) requires unweighting by multiplying by $1/f$. Interpolation of the fill fraction array $f(x, y)$ in POS coordinates to the RRSP grid introduces enough inaccuracies into the resulting array that multiplying by $1/f$ results in implausibly large values of magnetic field strengths and Poynting fluxes in some pixels. Consequently, we only report results from the POSSP data here. Throughout the remainder of the manuscript, values for magnetic fields given in units of Mx cm^{-2} refer to pixel-averaged flux densities, i.e., f -weighted, while values quoted in G refer to intrinsic field strengths.

The SP raster across the central part of the active region that is most closely aligned with the NFI FOV took slightly more than half an hour. Since the NFI magnetogram cadence was about two minutes, no single NFI magnetogram or velocity field is co-temporal with the SP magnetic field measurements. Figure 1 shows fB_z from the SP data in grayscale, with $\pm 250 \text{ Mx cm}^{-2}$ contours of B_{NFI} overplotted (black for flux toward the observer, white for away). Rastering for the SP observation was left-to-right, and the longer SP observing interval causes to some local discrepancies between the fields. (In this image, the x coordinates for contours of B_{NFI} were stretched by 1.01 from the SP data, necessary to compensate for a small discrepancy ($< 0.''01$) found between the NFI and interpolated SP pixel sizes.)

To analyze approximately simultaneous velocity and magnetic field data, we restrict our attention to the (51×51) pixel² area of plage to the east of the main sunspots in the region. The plage region that is the focus of our study in the white box at lower left of Figure 1. The scan across our plage region took about three minutes, from 20:46:47 – 20:49:56. We used the NFI image time stamped 20:48:20. While the SP vector-field estimates are given at plane-of-sky pixel locations, the magnetic field vectors were expressed in spherical coordinates (r, θ, ϕ) . We represent these vectors in a Cartesian coordinate system, with $B_z = B_r$, $B_y = -B_\theta$, and $B_x = B_\phi$. While this representation is somewhat inaccurate over the FOV of the whole active

SP, 2006/12/12, c.20:48; NFI contours

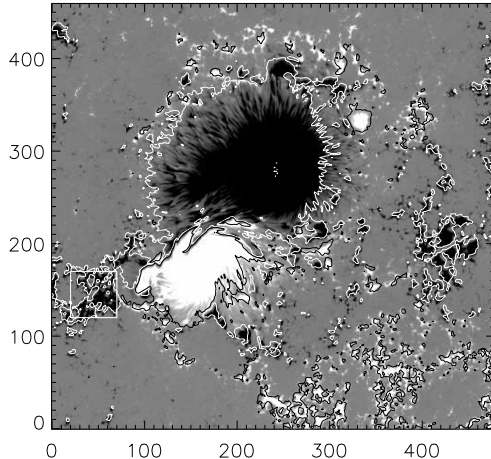


Fig. 1. Grayscale: fB_z from SP data (saturation at $\pm 750 \text{ Mx cm}^{-2}$), with $\pm 250 \text{ Mx cm}^{-2}$ contours of B_{NFI} overplotted (black for flux toward the observer, white for away). The plage region that is the focus of our study is in the white box at lower left. Rastering for the SP observation was left-to-right, and the observing duration was much longer for the SP data than for the NFI data, leading to some local discrepancies between the fields.

region, it is not problematic in the small area of plage that we study (about one heliocentric degree on a side).

In the (2×2) -binned NFI data, the plage region that we studied corresponds to $x \in [32, 82]$ and $y \in [140, 190]$. We roughly co-aligned the SP data by hand to within a few pixels, and then computed the cross-correlation of the nearly-aligned images to find the whole-pixel shift at the maximum of the cross-correlation function. To avoid introducing artifacts from interpolation, we only co-registered the data down to the pixel scale, and not smaller. Residual shifts for the SP data in (x, y) are $(-0.02, 0.23)$ pixels, respectively. To illustrate the co-alignment, we plot contours of B_{NFI} at ± 125 and $\pm 250 \text{ Mx cm}^{-2}$ over a grayscale image of f -weighted B_z from SP data in the plage region in the left panel of Figure 2. In the right panel, we show a scatter plot of filling-factor-weighted B_z from SP versus B_{NFI} . The linear and rank-order correlation coefficients (Press et al. 1992) are both 0.93; the similarity between both measures of correlation implies that outliers in B_{NFI} and B_z do not play a major role in the correlation.

A fit of B_{NFI} to the filling-factor-weighted B_z yields a slope near 0.69, implying weaker flux densities for B_{NFI} . Discrepancies could have arisen from both the more accurate polarimetric measurements in the SP data and evolution in the fields while the SP was rastered.

The mean and median vertical flux densities in this region are -434 Mx cm^{-2} and -354 Mx cm^{-2} , respectively. The mean unsigned B_z has the same magnitude as mean B_z , so the region really is unipolar. The mean and median horizontal f -weighted flux densities are 160

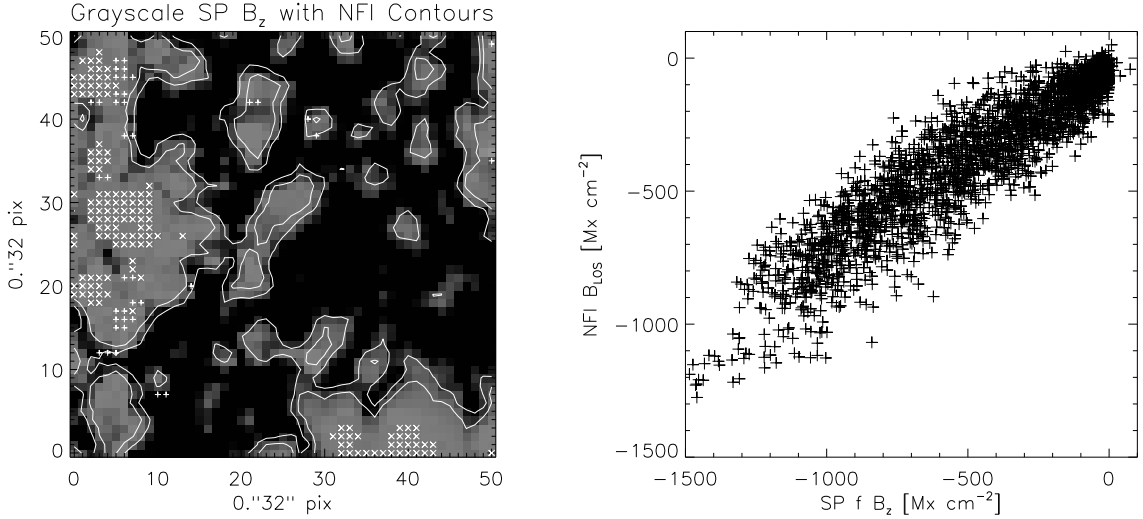


Fig. 2. Left: Contours of B_{NFI} at -125 and -250 Mx cm^{-2} over a grayscale image of fB_z from the SP data (saturation set to $\pm 500 \text{ Mx cm}^{-2}$) in the plage region in the left panel of Figure 1. Errors in \mathbf{B} were not estimated in pixels marked with \times , and were large in pixels marked with $+$. Right: a scatter plot of fB_z from SP data versus B_{NFI} . The rank-order and linear correlation coefficients are both 0.93.

Mx cm^{-2} and 121 Mx cm^{-2} , respectively. The larger values of the means compared to medians here imply that some field strengths are substantially larger than the bulk of the population. The mean and median inclination angles are similar, 154° and 157° , respectively — so 26° and 23° from vertical — implying the field in the bulk of the population is nearly vertical.

Error estimates for the vector magnetic field were derived by the ASP inversion code for the SP data in pixels at slit positions with sufficient polarization signal for reliable inversions, as described in Schrijver et al. 2008, and provided by B. Lites (private communication). In 139 of our 2601 pixels, error estimates were not made, corresponding to weak-field pixels; these are shown in the left panel of Figure 2 with \times symbols. In 40 pixels, error estimates were large, with errors in inclination and azimuth exceeding 180° and 360° , respectively. These are also shown in the left panel of Figure 2, but with $+$ symbols. Among the remaining 2422 pixels, the mean and standard deviation of uncertainties in field strength, inclination, and azimuth were $(47 \pm 38) \text{ G}$, $(2.1 \pm 2.3)^\circ$, and $(7.5 \pm 16)^\circ$. We performed simple Monte Carlo simulations to estimate uncertainties in (B_x, B_y, B_z) . In each run, for pixels with valid uncertainties (i.e., not the 179 pixels discussed above) we multiplied each pixel’s uncertainties in field strength, inclination, and azimuth by randomly generated, normally distributed coefficients (appropriately scaled to the estimated uncertainties), added the results to the original values, and projected the resulting vector into its (x, y, z) components. We then computed the mean of absolute differences between the perturbed and original values for that run. For 1000 runs, the uncertainties in (B_x, B_y, B_z) are $(30, 36, 35)$ gauss, respectively. The relatively large uncertainty in B_z probably results from our approach, which averages absolute errors, even though these might be small in fractional

terms for strong-field pixels B_z . This approach also ignores errors in ambiguity resolutions and filling factors.

We expect the impact of measurement errors in \mathbf{B} on S_z^{plage} to be relatively small in all summed results: since the quantities that are summed in equation (4) are signed (from the product of B_z with the dot product of \mathbf{B}_h with \mathbf{v}_h), some cancellation should occur.

2.3. Tracking the NFI Magnetograms

Welsch et al. (2012) used a tracking code, FLCT (Fisher & Welsch 2008), to estimate velocities for the NFI sequence we analyze here. Many tracking algorithms estimate spatial displacements of local structures between a pair of images separated in time by an interval Δt . Tracking methods then typically have at least two free parameters: the time difference Δt between images; and the size L of the local neighborhood (around each pixel for which a velocity is sought) in which structures between the two images are associated. Accordingly, we briefly discuss our tracking parameters.

In some cases, Δt is tightly constrained by the cadence of observations. If, however, cadences are relatively rapid compared to the expected time scale of evolution of image structures, then successive images are likely to differ only by the noise in each measurement, leading to propagation of noise into the velocity estimates (Welsch et al. 2012). Welsch et al. (2012) suggested that temporal consistency in successive flow maps is a good indicator of robustness in the velocity estimates. This can be achieved by extending Δt until significant magnetic evolution has occurred. Accordingly, the flows we analyze here were derived by tracking the full NFI FOV with $\Delta t = 8$ min. Also, the initial and final magnetograms were computed by applying a five-step boxcar average to the NFI magnetograms.

Tracking codes (or optical flow methods generally, including LCT, DAVE, and DAVE4VM; see Schuck 2008) typically estimate the flow in a given pixel using information about evolution in a “local” neighborhood — within a user-set length scale, L , that describes the “apodization window” or “aperture” size — around that pixel. Schuck (2006) noted that, in the presence of noise, information from several pixels is essential to prevent spurious fluctuations due to noise from obscuring actual physical displacements. Consequently, selecting too small a value for L can increase susceptibility to noise, since not enough pixels are used in estimating each local displacement. Flows smaller than a given scale L are, however, smoothed over by tracking codes. We therefore chose to analyze flow maps derived with $L = 4 \times 0.''32$ pixels (set by FLCT’s σ parameter, used in a Gaussian windowing function, $\propto \exp[-r^2/\sigma^2]$), which struck a balance between boosting correlations between successive flow maps (i.e., suggesting the flow estimates were robust) but not over-degrading the resolution of the magnetograms that were tracked.

We also attempt to minimize confusion of fluctuations due to noise in the input magnetograms with *bona fide* magnetic evolution by not estimating velocities in pixels below the

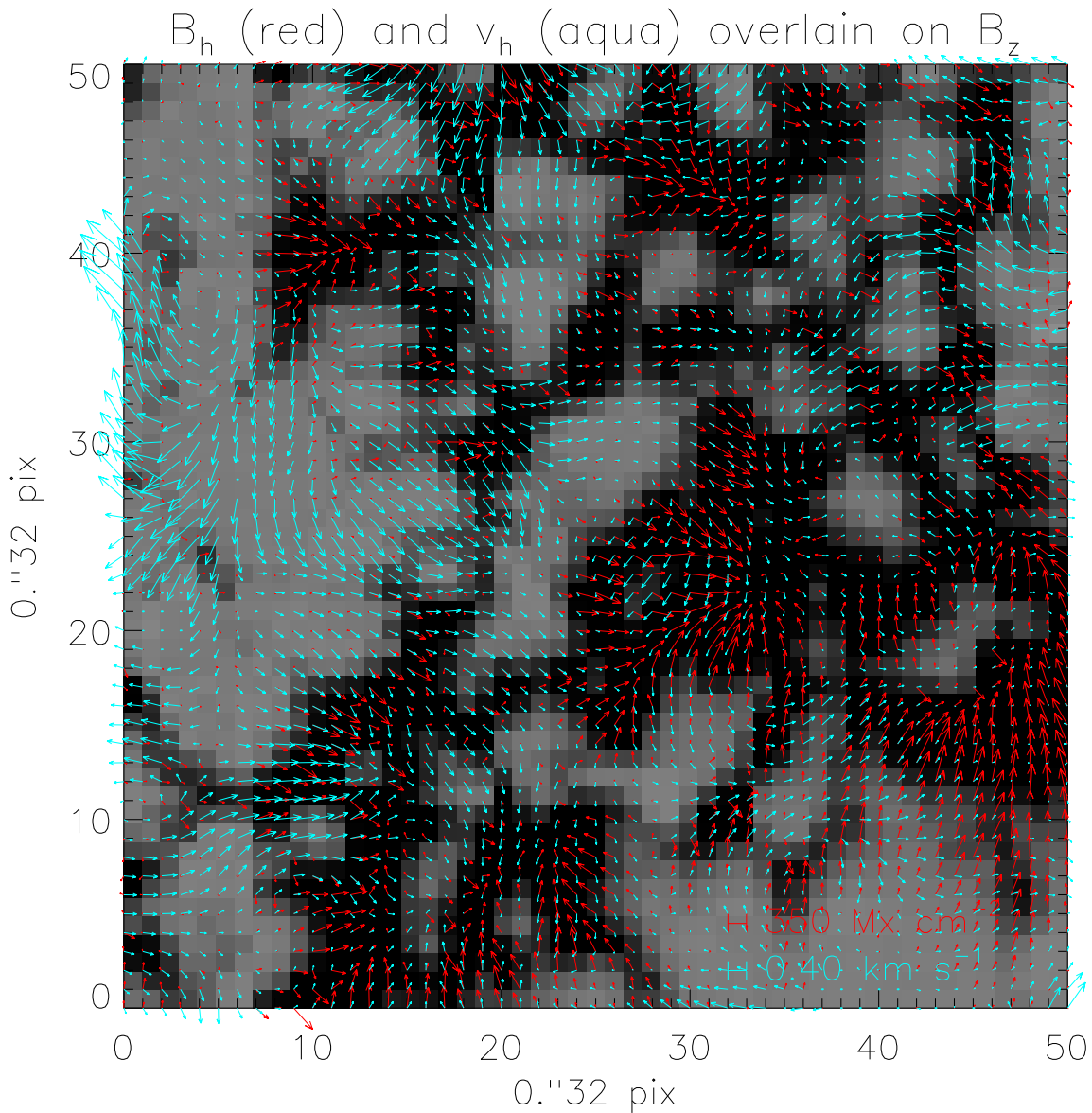


Fig. 3. Horizontal magnetic field (red) and FLCT velocities (aqua) overplotted on a grayscale image of fB_z (saturation at $\pm 750 \text{ Mx cm}^{-2}$). These three quantities are necessary ingredients for computing the Poynting flux via equation (4).

noise level. Accordingly, pixels in the NFI magnetograms with unsigned flux densities below the 15 Mx cm^{-2} noise level estimated by Welsch et al. (2012) were not tracked.

In Figure 3, we plot both horizontal magnetic field vectors, $f\mathbf{B}_h$, and FLCT flow vectors over a grayscale image of fB_z , for the flow map centered at 20:48:19. The mean and median horizontal FLCT speeds, in the 2,570 pixels in this field of view where estimates were made, are 0.17 km s^{-1} and 0.14 km s^{-1} , respectively.

Velocities tend to be larger in weaker-field regions, consistent with the general tendency of strong vertical fields to suppress convection (Title et al. 1992; Berger et al. 1998; Bercik

2002; Welsch et al. 2009; Welsch et al. 2012; Welsch et al. 2013; Kano et al. 2014). Kano et al. (2014) reported an anti-correlation between filling factor and the variance in flow speeds inferred from LCT. We also found such an anticorrelation in the plage region studied here: in the 2,414 pixels in which a speed was estimated and the fill fraction was not 1.0, linear and rank-order correlations between speeds and fill fractions were both -0.18. (As noted in §3.3 below, this value is statistically significant.) Anticorrelations were also found between speeds and each of intrinsic field strength, intrinsic $|B_z|$, and intrinsic $|\mathbf{B}_h|$; but the anticorrelations were weaker than that of speed with f , suggesting that fill fraction is the principal correlated factor.

As a check upon our results, we also tracked the full NFI FOV with a separate LCT code, one provided by Y.-J. Moon (private communication) that has been used in other published work (e.g., Moon et al. 2002). While FLCT computes the cross-correlation function in Fourier space, this second tracking code computes the correlation function in regular space, following November & Simon (1988). Hence, we refer to it as Spatial LCT (SLCT), in contrast to Fourier LCT. We also only tracked pixels with absolute flux density above 15 Mx cm^{-2} , with the same Δt , but set σ in this code to 3 pixels, since its weighting function includes a factor of 2 in the denominator of the exponential, $\propto \exp(-r^2/2\sigma^2)$. This routine returned either excessively large velocities in some pixels or even NaNs (in 4% of tracked pixels). Velocities in excess of 2 km s^{-1} ($< 1.5\%$ of tracked pixels) or equal to NaN were set to zero.

In the left panel of Figure 4, we show SLCT velocities overlain on B_z . Comparison of these flows with those in Figure 3 shows rough agreement in many places, but also clear disagreements in others. Rank-order correlation coefficients between these methods' v_x and v_y values in pixels where both methods made valid estimates were 0.85 and 0.77, respectively. Linear correlations were similar, at 0.85 and 0.63 for v_x and v_y , respectively. Linear and rank-order correlations near 0.8 result from adding 10% random variation to a flow component and then correlating it with the unperturbed flow component. This suggests about $\sim 10\%$ variability in estimated flows due to the LCT implementation. Consistent with these significant correlations, a scatter plot in the right panel of Figure 4 shows that the flows are substantially correlated. The mean and median horizontal SLCT velocities, among pixels where valid estimates were made, are 0.15 km s^{-1} and 0.13 km s^{-1} , respectively, quite close to the values for FLCT.

3. Results

3.1. Poynting Fluxes

We combined the FLCT flows estimated from the NFI data with the co-registered vector magnetic field data and fill fraction from SP in equation (4) to compute the Poynting flux averaged over the plage region. We find a net positive average Poynting flux, $S_z^{\text{plage, FLCT}} = 4.9 \times 10^7 \text{ erg cm}^{-2} \text{ s}^{-1}$. In Figure 5, we show a grayscale map of the Poynting flux, with

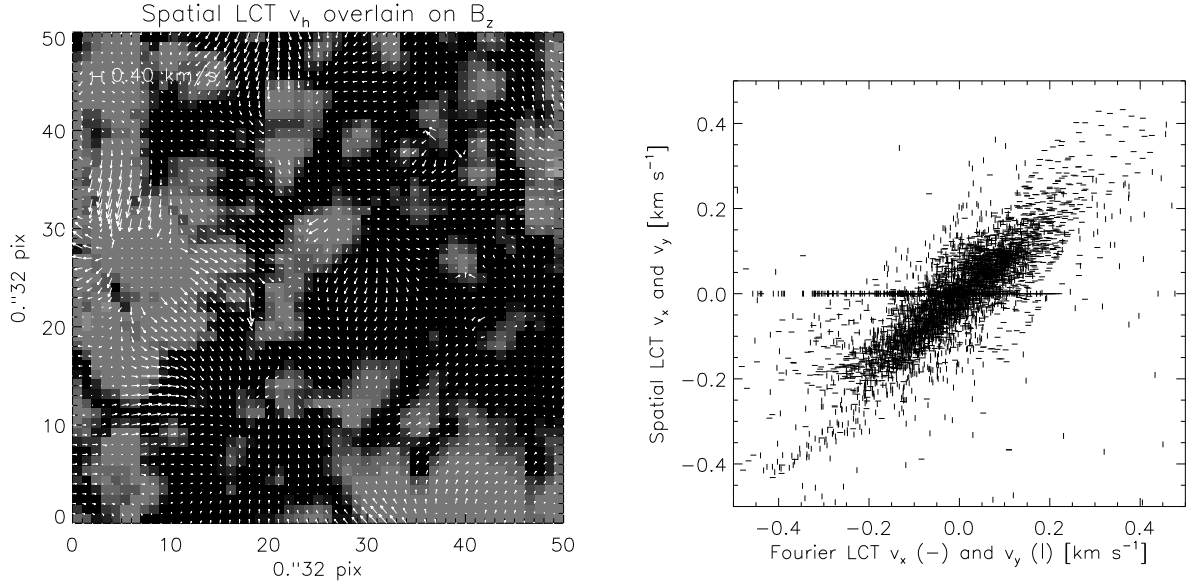


Fig. 4. Left: SLCT velocity vectors overplotted on a grayscale image of fB_z (saturation at $\pm 500 \text{ Mx cm}^{-2}$) from SP. Right: A scatter plot comparing v_x (—'s) and v_y (|'s) from FLCT and SLCT.

saturation set to $\pm 4 \times 10^8 \text{ erg cm}^{-2} \text{ s}^{-1}$, overlain with -125 Mx cm^{-2} and -250 Mx cm^{-2} contours of fB_z from the SP data. Regions with both positive and negative Poynting flux are visible, but the net Poynting flux is positive. Using the SLCT flows, we also find a net positive Poynting flux, but estimate $S_z^{\text{plage,SLCT}} = 5.5 \times 10^7 \text{ erg cm}^{-2} \text{ s}^{-1}$. This is about 12% larger than the FLCT result. The fractional difference between FLCT and SLCT results, compared to their average, is about 6%. The Poynting flux maps are significantly correlated, with pixel-wise linear and rank-order correlations of 0.90 and 0.85 in pixels where both methods made estimates. Evidently, the flow estimation process is a source of at least a $\sim 10\%$ uncertainty in our estimates. Further study of this same data set, using a different tracking method (e.g., DAVE or DAVE4VM; Schuck 2006, Schuck 2008) would be worthwhile.

Based upon tests of flow reconstruction methods by Welsch et al. (2007), it is not surprising that different flow methods yield somewhat different results. Flows from most of the methods tested by Welsch et al. (2007) were significantly correlated with both each other and with the true flows. But flows from the various methods did not agree closely, and most of the methods only recovered a fraction of the Poynting flux. Results about Poynting fluxes from the tests by Welsch et al. (2007), however, are probably not applicable here, because the rising-flux-tube magnetic geometry in the MHD data they used is very different than our plage region: their field was primarily horizontal, and the Poynting flux was dominated by the emergence term, not the shearing term. For pixels in the upper 95% of the distribution in $|B_z|$ (the criterion they used to determine the population they tracked), this can be seen in a number of statistical measures: the median horizontal field was five times stronger than the median vertical field; the mean and median inclination angles (from the vertical) were both

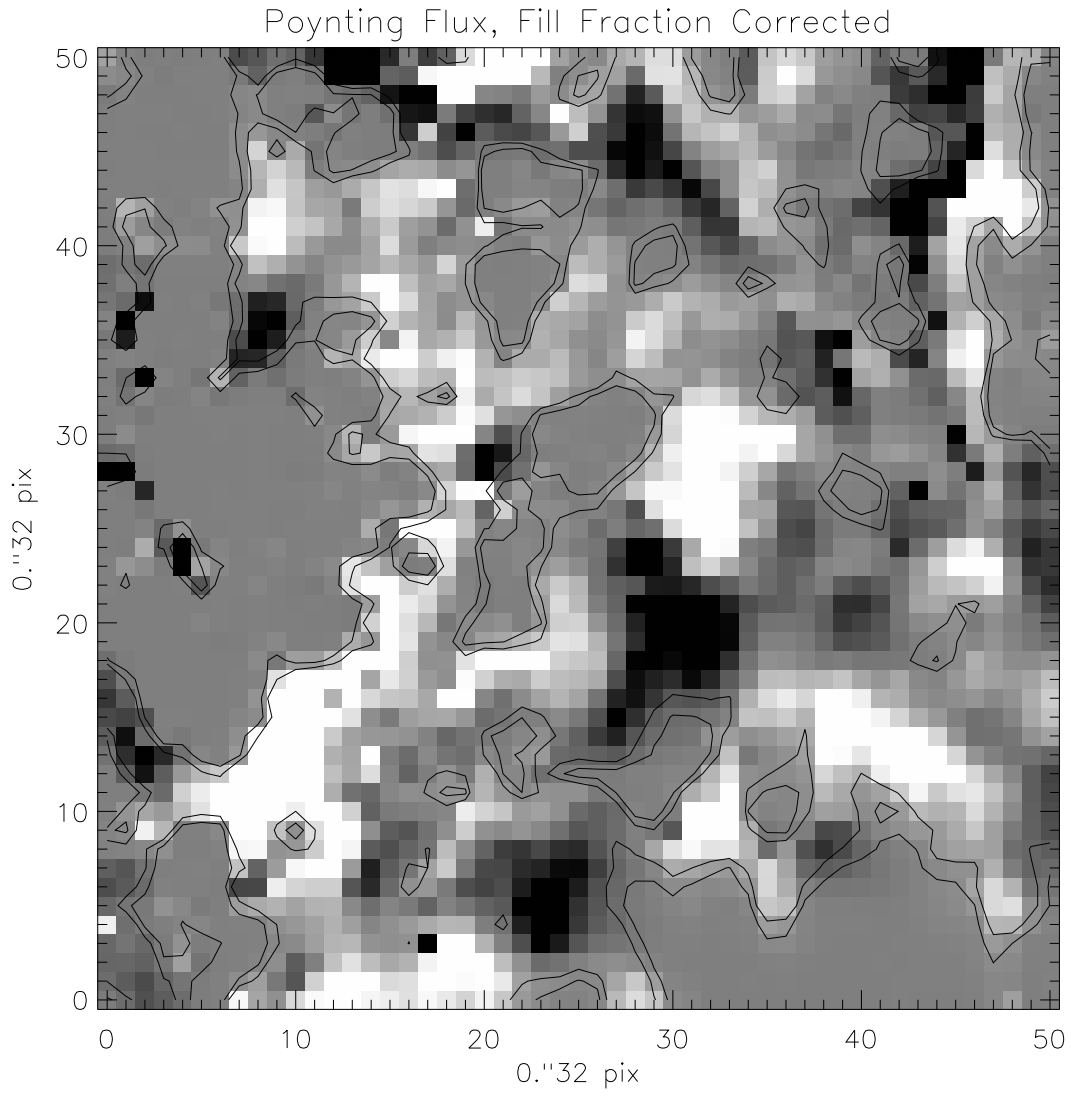


Fig. 5. The grayscale map shows the Poynting flux, with saturation set to $\pm 4 \times 10^8 \text{ erg cm}^{-2} \text{ s}^{-1}$, overlain with -125 Mx cm^{-2} and -250 Mx cm^{-2} contours of fB_z . Regions with both positive and negative Poynting flux are visible, but the net Poynting flux is positive.

larger than 65° ; and the emergence term in the Poynting flux was largest in every pixel above their tracking 5% threshold (and in 99% of all pixels).

To characterize the uncertainty in our Poynting flux estimate due to uncertainties in the magnetic fields, we also employed the Monte Carlo approach described in §2.2 above to calculate the effect of magnetic fields components perturbed by the inversion uncertainties on the Poynting flux computed via (4). Excluding the 179 pixels with invalid error estimates from these Poynting flux calculations, in 1000 runs of randomly perturbed magnetic fields, we find the mean and standard deviation of the Poynting flux to be $(5.2 \pm 0.1) \times 10^7 \text{ erg cm}^{-2} \text{ s}^{-1}$. If we use the same approach, but substitute the mean uncertainty estimates from all other pixels for the 179 pixels with excessive errors, then for 1000 runs we find a mean and standard deviation of the Poynting flux of $(4.9 \pm 0.1) \times 10^7 \text{ erg cm}^{-2} \text{ s}^{-1}$. This suggests that uncertainties in the estimated magnetic fields are a relatively small part of the overall uncertainty in the Poynting flux.

In Figure 5, many values of the Poynting flux are much larger than the average value. Could the upward average energy be an accident, due simply to excess Poynting flux from a few pixels with large values? The distribution of Poynting flux values suggests that the net upward flux arises from a statistical predominance of upward fluxes in the high-Poynting-flux wings of the distribution. This can be seen in Figure 6, where we plot histograms of the upward (solid) and downward (dotted) Poynting flux, taken from the map in Figure 5. As may be seen, there is a prevalence of pixels with upward-directed Poynting fluxes at high-Poynting-flux values.

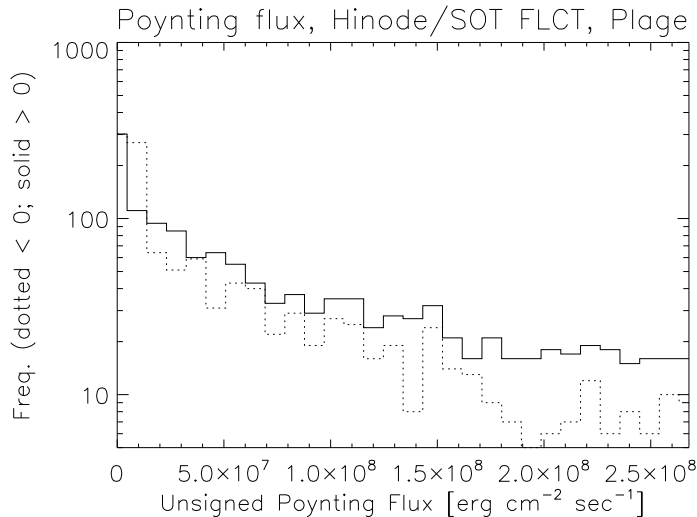


Fig. 6. Histograms of the upward (solid) and downward (dotted) Poynting fluxes, taken from the map Figure 5. In pixels with high values of unsigned Poynting flux, upward-directed fluxes outnumber downward-directed fluxes. This statistical bias suggests that the net-positive Poynting flux over the FOV did not arise randomly, due to just a few pixels.

The dependence of the mean Poynting flux on the wings of the distribution implies that

the standard deviation of the Poynting flux values is not a good estimator of the standard error of the mean (i.e., the uncertainty in our estimate of the mean). To estimate the standard error in the mean, we computed 10^4 bootstrap samples (Press et al. 1992), which had a mean Poynting flux of $5.0 \times 10^7 \text{ erg cm}^{-2} \text{ s}^{-1}$ and a standard deviation of $5 \times 10^6 \text{ erg cm}^{-2} \text{ s}^{-1}$. (Note that this mean is over the subset of pixels with non-zero Poynting flux estimates; the value of $4.9 \times 10^7 \text{ erg cm}^{-2} \text{ s}^{-1}$ cited above is over the entire 2601 pixels in our plage region.) It should be noted, however, that since FLCT's σ was set to 4 pixels, the data are not strictly independent: the flows are correlated below this scale. The magnetic fields also exhibit structure on a similar scale. Consequently, the assumption of independent data points that underlies the bootstrap approach is probably violated here, since neighboring pixels tend to be similar. This test does, however, demonstrate that the mean Poynting flux we that report does not depend upon values in just a few pixels, because we found very similar mean values even when resampling the population of Poynting flux values.

Considering the variation in estimated Poynting flux indicated by the differing tracking methods ($\sim 6 \times 10^6 \text{ erg cm}^{-2} \text{ s}^{-1}$) and the bootstrap runs (again, $\sim 5 \times 10^6 \text{ erg cm}^{-2} \text{ s}^{-1}$), we estimate the overall uncertainty level to be on the order of $1 \times 10^7 \text{ erg cm}^{-2} \text{ s}^{-1}$.

One aspect of the Poynting flux map in Figure 5 is notable: upward and downward energy fluxes appear bipolar in some areas (e.g., near pixel coordinates [30,25], [30,45], and [45,45]). Inspection of the same regions in Figure 3 shows that these bipolar structures arise when horizontal magnetic fields change direction (e.g., converge) within an area of horizontal flows that are more uniform on the same spatial scale. Qualitatively, this does not accord with the simplistic picture of braiding of sub-resolution, elemental flux tubes proposed by Parker (1983): a substantial Poynting flux is spatially resolved, and we do not see fluxes winding about each other. (We discuss vorticities in both the flow and magnetic fields in §3.3, below).

We note that the average Poynting flux that we obtain for this plage region is substantially larger than the value of $1.7 \times 10^7 \text{ erg cm}^{-2} \text{ s}^{-1}$ obtained by Yeates et al. (2014) for a different plage region. Inclusion of the $1/f$ factor in our estimate certainly explains much of the difference. Without this factor, our average Poynting flux would be just $2.7 \times 10^7 \text{ erg cm}^{-2} \text{ s}^{-1}$, still a factor of 1.6 larger than that reported by Yeates et al. (2014). We note that the mean and median unsigned vertical fields in our plage region (434 Mx cm^{-2} and 354 Mx cm^{-2} , resp.) are larger than the corresponding values in the region studied by Yeates et al. (2014) (365 Mx cm^{-2} and 274 Mx cm^{-2} , resp.) by factors of ~ 1.3 . So differing field strengths might explain some of the disparity.

While magnetograms of the full NFI FOV were co-aligned prior to tracking (Welsch et al. 2012), it is still possible that mean motion of the plage region we study here, combined with a mean horizontal magnetic field in the region, could produce the mean Poynting flux we find. To investigate this possibility, we computed a region-averaged Poynting flux, \bar{S}_z^{plage} , given by

$$\bar{S}_z^{\text{plage}} = -\langle \mathbf{v}_h \rangle \cdot \langle \mathbf{B}_h \rangle \langle B_z \rangle / (4\pi) , \quad (5)$$

where the angle brackets denote averaging over the (51×51) pixel plage region, and fill-fraction-weighted magnetic field values (i.e., pixel-averaged values) were used in the averages. For FLCT and SLCT flows, we find $\bar{S}_z^{\text{plage,FLCT}} = -2.7 \times 10^6 \text{ erg cm}^{-2} \text{ s}^{-1}$ and $\bar{S}_z^{\text{plage,SLCT}} = -2.3 \times 10^6 \text{ erg cm}^{-2} \text{ s}^{-1}$. These region-averaged values are significantly smaller than and opposite in sign to the net Poynting fluxes we find above.

3.2. Poynting Fluxes in Other Plage Regions

Is the systematic prevalence of pixels with upward Poynting flux seen in Figure 6 a fluke, or is it the norm? To settle this question, it would be helpful to analyze the Poynting flux in other plage regions.

As noted above, however, the different cadences of the SP raster used to measure \mathbf{B} and the NFI magnetograms tracked to infer \mathbf{v}_h imply that no single velocity measurement is simultaneous with the vector magnetic field measurement across the region. So we cannot simply apply equation (4) across the active region. This motivated our focus, above, on a relatively small patch of plage, for which estimates of \mathbf{B} and \mathbf{v}_h were nearly simultaneous.

To work around the simultaneity issue, “rastered” 2D arrays (in x and y) of $v_x(x, y)$ and $v_y(x, y)$ were constructed, by selecting each column of the 2D array for each velocity component from the time-slice of the 3D datacubes (in x, y, t) of velocities closest in time to when the SP measurement was made at the corresponding column. This enables estimating the Poynting flux from the shearing term over most of the active region (though data near the top of the FOV is excluded due to the “bubble” in NFI).

Since our focus is on the shearing Poynting flux in plage regions, we define a mask of “plage-like” pixels. We set this 2D bitmap to 1 for all pixels with filling-factor-weighted $|B_z|$ between 100 and 1500 Mx cm⁻² and inclinations of less than 30 from the vertical, and for which fill fractions were estimated. (Inversions were not performed for all pixels; fill fractions were not estimated in non-inverted pixels. The field in non-inverted regions with significant Stokes’ V signals was assumed vertical.) Figure 7 shows fB_z across most of the active region in grayscale, with contours of the plage-like pixel mask overplotted. We use the term “plage-like” because our criteria for plage identification are imperfect: a few small regions very near the positive and negative umbrae satisfy the plage-like criteria, along with many very small isolated clumps of quiet-sun fields. Both of these classes of pixels would probably not be identified as plage by a human observer. Our approach does, however, capture the majority of plage magnetic field regions across the active region. Further, it is objective, meaning it can be systematically applied, whereas identifications made by human observers would be subjective.

Figure 8 shows the distributions of upward and downward Poynting fluxes for all plage-like pixels across AR 10930. As with the distributions from the (51×51) pixel² region shown in Figure 6, the frequency of pixels with upward Poynting flux is systematically higher than

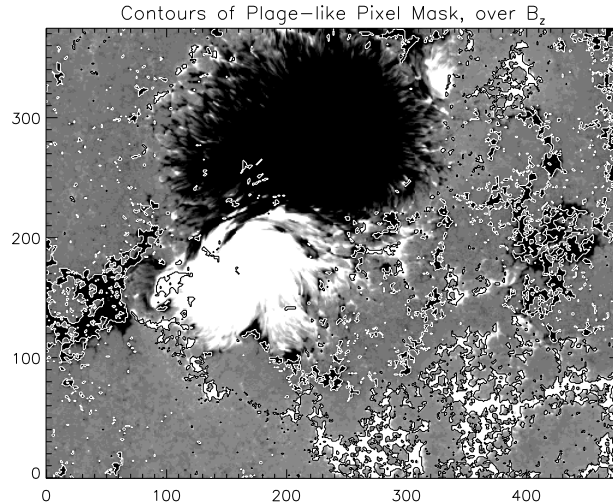


Fig. 7. Grayscale shows fB_z over much of AR 10930, with saturation set to $\pm 250 \text{ Mx cm}^{-2}$. Contours outline regions of “plage-like” pixels (white around negative-flux regions, black around positive-flux regions), which have absolute field strengths between 100 and 1500 Mx cm^{-2} and inclinations of less than 30° from the vertical, and for which fill fractions were estimated (see text).

that of pixels with downward Poynting flux. The systematic difference between upward and

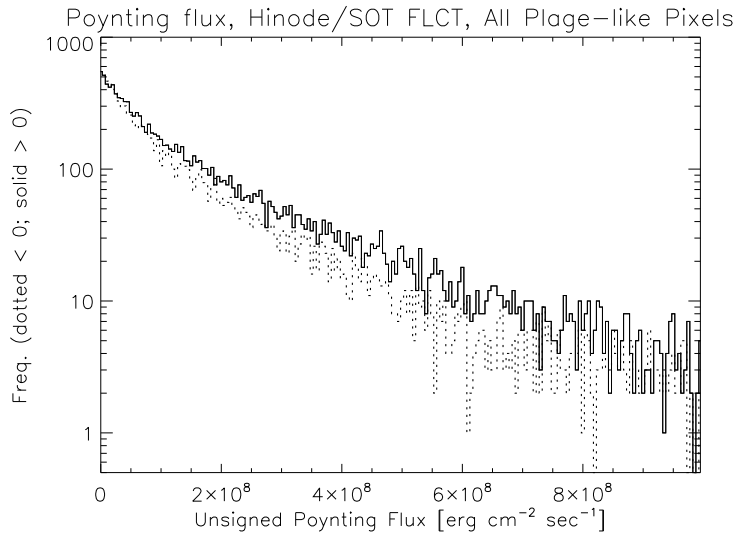


Fig. 8. Histograms of the upward (thin solid) and downward (thick dotted) Poynting fluxes from all plage-like pixels (i.e., those within the contours in Figure 7) that we identified in AR 10930. A systematic bias is evident in the frequencies, with upward-flux pixels outnumbering downward-flux pixels across most of the distribution. The systematic discrepancy between upward and downward energy fluxes is consistent with losses due to atmospheric heating.

downward energy fluxes should correspond to losses of some kind, perhaps due to atmospheric heating processes.

Given the sparse nature of the plage-like pixel mask, and the utility of closely examining dynamics and magnetic field structure in a sample plage region, we turn our attention again to the (51×51) pixel² region that has been our focus.

3.3. Dependence on Magnetic Structure

Investigating relationships of magnetic field and flow properties with the Poynting flux can improve our understanding of the physical processes that generate Poynting fluxes. In analogous efforts to understand coronal heating, Golub et al. (1980) found a clear relationship between the presence of photospheric magnetic flux and coronal soft-X-ray (SXR) emission, and Fisher et al. (1998) investigated relationships between SXR luminosity L_x and global properties of photospheric magnetic fields several hundred active regions in Haleakala Stokes Polarimeter vector magnetograms. Quantities they analyzed included total unsigned magnetic flux, total unsigned vertical electric current, and average field strength. Despite expectations that electric currents should play a role in the heating that powers coronal SXR emission, they found that the regions' luminosities depended more strongly on their total unsigned magnetic flux, Φ , than any other global magnetic variable they considered. Further, they found that L_x scaled as a power law in Φ , with an index near one. Pevtsov et al. (2003) then showed that the magnetic flux vs. soft X-ray luminosity correlation holds over a wide range of magnetic scales for the Sun — from X-ray bright points to whole active regions to the entire disk — and even other stars. (See also Fludra and Ireland [2008], who found power laws between whole-AR EUV intensities and magnetic fluxes.)

We now apply a similar approach here, but to energy input (the Poynting flux) as opposed to output (SXR and EUV radiation), and investigate relationships of magnetic field and flow structure with the Poynting flux, with the aim of better understanding how Poynting fluxes arise. For context when considering other variables, we first consider baseline correlations between the magnetic field and the Poynting flux in our (51×51) pixel² box. For this, we only consider correlations for the 2560 pixels (of 2601 total) in which the velocity was estimated. Uncertainties in correlation coefficients can be computed using Fisher's z-transformation, and the standard error scales like $1/\sqrt{N}$ for correlation coefficients that are not close to ± 1 . For our sample, the standard error is about 0.02, so correlations larger than 0.06 in magnitude correspond to greater than 3σ departures from the null hypothesis of zero correlation. Since atypical values for our variables can arise in our data through errors in the inferred \mathbf{B} , \mathbf{v}_h , and f , as well as co-registration, we give rank-order correlation coefficients, since these are more robust against outliers.

Regarding the *unsigned* Poynting flux, we find stronger fields tend to produce stronger Poynting fluxes. Correlations between $|S_z^{\text{plage}}|$ (from FLCT) and the intrinsic magnetic variables $|\mathbf{B}|$, $|\mathbf{B}_h|$, and $|B_z|$ were 0.65, 0.54, and 0.57, respectively. For pixel-averaged values (i.e., f -weighted) of the same variables, the correlations for all three were larger, 0.72, 0.73, and 0.70.

The correlation with fill fraction was positive, at 0.22, suggesting that while flows might be suppressed in pixels with higher filling factor (as noted above), the stronger fields that tend to be present lead to larger Poynting fluxes.

What about correlations with the *signed* Poynting flux, S_z^{plage} ? Based upon the statistical imbalance in the distributions of upward versus downward Poynting fluxes, visible in Figures 6 and 8, any variables correlated with $|S_z^{\text{plage}}|$ (which is the parent distribution of the positive- and negative-Poynting-flux sub-populations) plausibly also exhibit some correlation with S_z^{plage} (the dominant sub-population). This suggests that sites of larger unsigned Poynting flux should, statistically, tend have an upward flux, implying the variables above should also be correlated with S_z^{plage} , albeit more weakly than with $|S_z^{\text{plage}}|$. Consistent with this idea, we found correlations with the intrinsic magnetic variables $|\mathbf{B}|$, $|\mathbf{B}_h|$, and $|B_z|$ to be 0.12, 0.20, and 0.09, respectively, while correlations with the corresponding f -weighted variables were 0.18, 0.22, and 0.16, respectively.

Compared to correlations with the magnetic field itself, correlations with the resolved spatial structure of the magnetic field were weak. If energy were crossing the photosphere in regions of significant vertical electric currents, then there should be a strong correlation between the Poynting flux and the unsigned horizontal curl of the f -weighted horizontal photospheric field ($|\hat{\mathbf{z}} \cdot (\nabla_h \times \mathbf{B}_h)|$, which is $\propto |J_z|$ by Ampère’s law). The correlation with $|S_z^{\text{plage}}|$ that we found, however, was just 0.13 — while significant, this was much weaker than the baseline correlations with the magnetic field itself. The correlation of $|S_z^{\text{plage}}|$ with the unsigned, f -weighted horizontal divergence of the horizontal field ($|\nabla_h \cdot \mathbf{B}_h|$) was significantly stronger at 0.28, but also relatively weak compared to the baseline magnetic correlations. (This divergence should correspond to the magnetic field structure in “azimuth centers,” albeit for centers on smaller scales than reported by Martinez-Pillet et al. 1997.) Perhaps unsurprisingly, the correlations between *signed* Poynting flux, S_z^{plage} , and these the unsigned horizontal curl and divergence of \mathbf{B} were even weaker, at 0.04 and 0.07 — only marginally significant.

What about correlations between flow properties and the Poynting flux? First, we found correlations of $|\mathbf{v}_h|$ with $|S_z^{\text{plage}}|$ and S_z^{plage} of 0.13 and 0.06, respectively. The anti-correlation between filling factor and speed discussed above, and the dependence of the Poynting flux on the direction of \mathbf{v}_h probably both contribute to this weak dependence on speed.

We also present some of scatter plots relating some pairs of these quantities in Figure 9. The scatter plots of S_z^{plage} with intrinsic field strength (upper left), filling factor (upper right), and speed (bottom left) show a trend for increasing Poynting fluxes (regardless of sign) as each of these variables increases. Also, points with large, positive values of S_z^{plage} tend to outnumber points with large, negative values of S_z^{plage} as each of these variables increases. The scatter plot of speed as a function of fill fraction does show a tendency for higher-speed flows in pixels with lower fill fractions.

Vortical motions could play a role in energy transport into the outer solar atmosphere

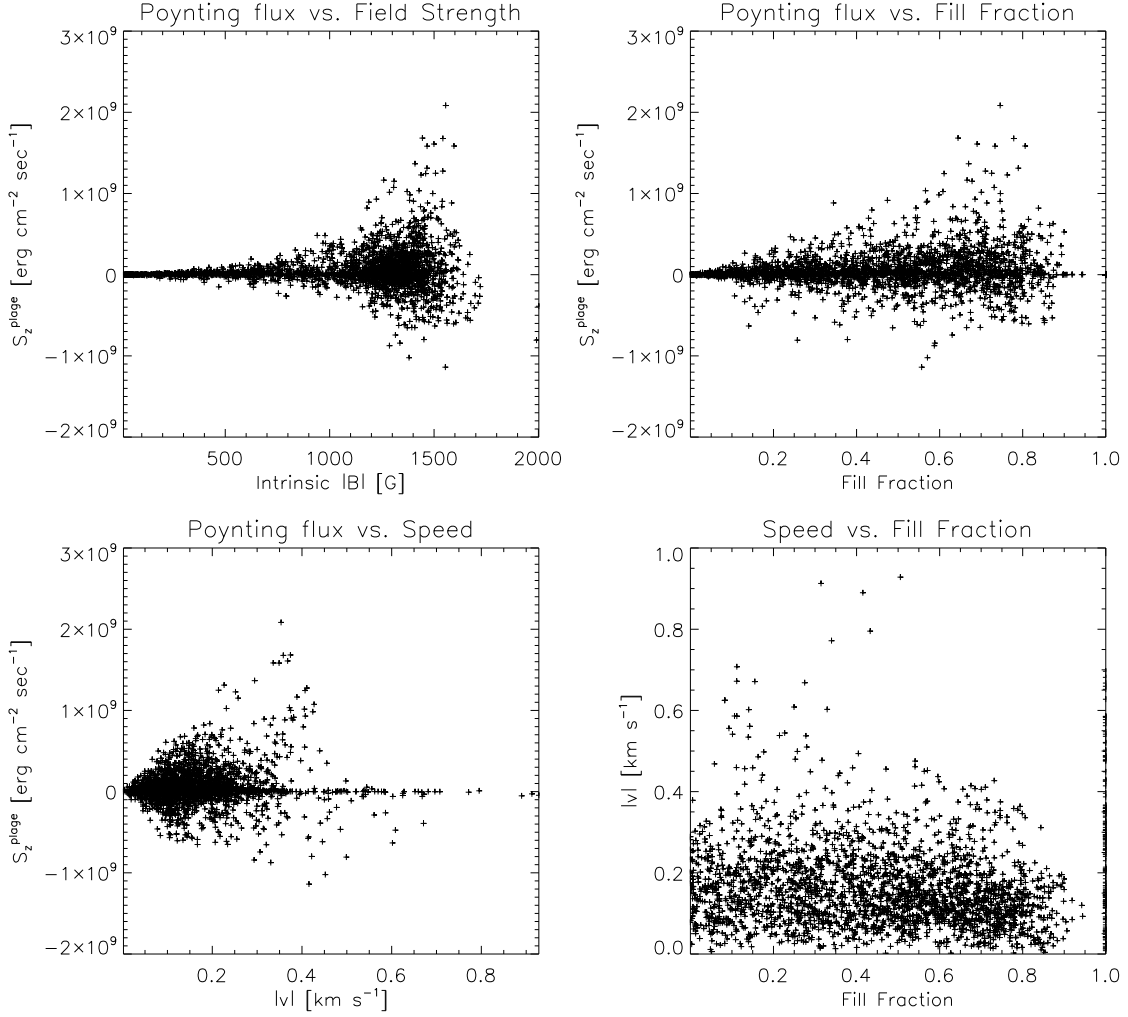


Fig. 9. Scatter plots of the signed Poynting flux with: intrinsic field strength, $|\mathbf{B}|$ (upper left); filling factor, f (upper right); and speed, $|\mathbf{v}|$ (bottom left). Bottom right: scatter plot of speed with fill fraction.

(e.g., Parker 1983, Kitiashvili et al. 2014), but we also found relatively weak correlations between unsigned vorticity, $|\hat{\mathbf{z}} \cdot (\nabla_h \times \mathbf{v}_h)|$, and $|S_z^{\text{plage}}|$ and S_z^{plage} of -0.09 and 0.04, respectively. Hence, we find little evidence for resolved vortical flows playing a significant role in driving Poynting fluxes. It should be borne in mind, however, that the spatial scale of resolved by LCT methods is larger than that of the images that are tracked — $\sim 1''$ versus $0.''32$ in our case.

It is also possible that converging (or diverging) flows might inject (or remove) magnetic energy by concentrating (or dispersing) magnetic flux. We checked this by correlating $-(\nabla_h \cdot \mathbf{v}_h)$, which should be positive for converging flows, with $|S_z^{\text{plage}}|$ and S_z^{plage} ; both were basically insignificant at 0.03 and 0.02, respectively. Correlations with the unsigned horizontal divergence of \mathbf{v}_h were not larger.

It is also worthwhile to characterize the signed energy *input* per unit of magnetic flux, based upon the reported nearly linear scalings of energy *output* in SXR (Fisher et al. 1998;

Pevtsov et al. 2003) and EUV (Fludra & Ireland 2008) luminosities per unit magnetic flux. Accordingly, we now compute quantities with units consistent with a ratio of luminosity per maxwell of $|B_z|$. For each pixel that was tracked with FLCT, we computed the ratio of signed energy input per maxwell. The mean and median of the ratios in this set of pixels were 1.11×10^5 erg s⁻¹ Mx⁻¹ and 6.6×10^4 erg s⁻¹ Mx⁻¹, respectively. Totaling the energy input and unsigned magnetic flux separately, and then dividing — i.e., computing the ratio of sums instead of the sum of ratios used to compute the mean above — yields a value of 1.12×10^5 erg s⁻¹ Mx⁻¹ for the whole-FOV energy input per maxwell. Pevtsov et al. (2003) report SXR luminosities of roughly 10^3 erg s⁻¹ Mx⁻¹. Order-of-magnitude estimates of SXR luminosity L_x as a fraction of total radiated energy from heating L_{heat} suggest $L_x \sim 10^{-2} L_{\text{heat}}$ (Longcope 2004; Schwadron et al. 2006). If the energy fluxes of $\sim 10^5$ erg s⁻¹ Mx⁻¹ that we find are fully thermalized, and these order-of-magnitude estimates are correct, then our results are approximately consistent with those of Pevtsov et al. (2003). Studies of additional plage regions would be worthwhile, to determine if our value of $\sim 10^5$ erg s⁻¹ Mx⁻¹ is typical.

As we have seen, stronger-field pixels tend to have larger Poynting fluxes, although in the case of the signed Poynting flux, the correlation is relatively weak. The tendency of magnetic fields to inhibit convection (Title et al. 1992; Berger et al. 1998; Bercik 2002; Welsch et al. 2009; Welsch et al. 2012; Welsch et al. 2013; Kano et al. 2014) might explain the this weak correlation: a turning point could be reached as field strength increases, beyond which increasingly weak convective velocities produce a smaller convection-driven Poynting flux. This is a plausible explanation for the relative darkness of the corona in EUV and SXR images directly above sunspot umbrae. (Note, however, that spatially coherent, large-scale flows, like those in rotating sunspots [e.g., Brown et al. 2003], could still easily transport large amounts of magnetic energy across the photosphere in sunspot fields, though this energy might be more relevant to flares and CMEs than to coronal heating.) These considerations raise two related questions. First, what is the average (signed) Poynting flux as a function of field strength? And second, since some field strengths are more common than others, which part of the field strength distribution contributes the bulk of the Poynting flux? To address these questions, we first created a histogram of vertical field strengths, shown in the top panel of Figure 10. A clear peak is seen near 1300 G in $|B_z|$. We then computed the average and total (signed) Poynting fluxes in each bin (middle and bottom panels, respectively). From the bottom panel, it can be seen that the bulk of the total Poynting flux comes from pixels with vertical field strengths around the peak of the vertical field strength distribution. The middle panel shows, however, that weaker fields, on average, produce a similar Poynting flux, implying that their smaller contribution to the total energy flux is due to the relative dearth of such field strengths. Weaker fields might have average Poynting fluxes as high as stronger fields because higher velocities tend to be present in the former.

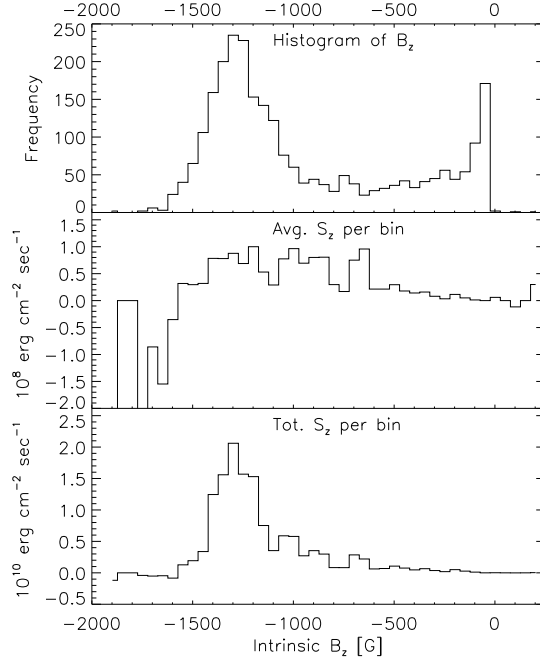


Fig. 10. Top: A histogram of vertical intrinsic field strengths, with clear peak near $|B_z| = 1300$ G. Middle: The average of (signed) Poynting fluxes over pixels with field strengths in each bin. Bottom: The sum of (signed) Poynting fluxes over pixels with field strengths in each bin. The bulk of the contribution to the total Poynting flux originates from pixels with vertical field strengths near the peak at 1300 G, but pixels with a range of vertical field strengths produce, on average, similar Poynting fluxes.

3.4. Comparison with Chromospheric Emission

It is plausible that regions of enhanced magnetic energy flux across the photosphere would be brighter in some form of emission. (It is also possible that the solar atmosphere above the photosphere could store injected magnetic energy, in the form of electric currents, for some time prior to its dissipation and consequent enhancement of emission. Another possibility is that the energy might propagate away from the site of its introduction, to be dissipated elsewhere.)

The plage region we analyze here was also observed in Ca II (H line) by the BFI, so we briefly investigate correlations of the Poynting flux map and other photospheric magnetic variables with this emission. The closest image in time to the NFI velocity estimate was recorded at 20:48:16 UT on 2006/12/12, which we co-registered with B_{NFI} after downsampling from the BFI pixel size of $0.''11$ by a factor of three to approximately match the $0.''32$ scale of our magnetic field and velocity arrays. In Figure 11, we show ± 125 and ± 250 Mx cm^{-2} contours of f -weighted B_z flux density overlain on the Ca II intensity in our (51×51) -pixel² plage region.

We now investigate correlations of Ca II intensity with magnetic and velocity field prop-

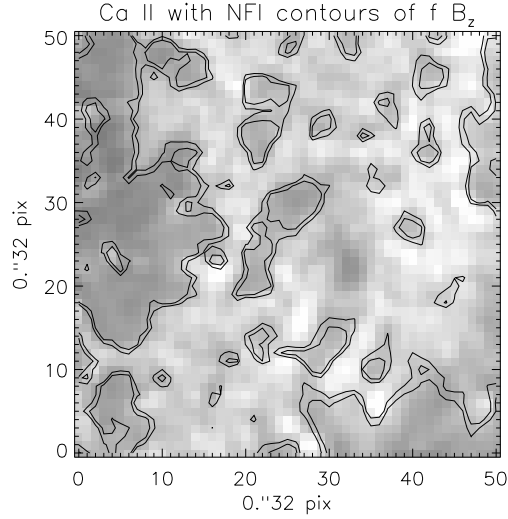


Fig. 11. ± 125 and ± 250 Mx cm^{-2} contours of f -weighted B_z from SP density are overlain on down-sampled Ca II intensity from BFI over our plage region.

erties, including the Poynting flux, to discover any interesting relationships. For magnetic variables, the spatial map of Ca II intensity exhibited the strongest correlations with $|B_z|$ and $|\mathbf{B}|$, which were greater than 0.6 for both intrinsic and pixel-averaged field strengths. The correlation with $|\mathbf{B}_h|$ was significantly weaker, at 0.22 and 0.46 for intrinsic and pixel-averaged field strengths, respectively. Correlations with the horizontal curl of f -weighted \mathbf{B}_h , $|\hat{\mathbf{z}} \cdot (\nabla_h \times \mathbf{B}_h)|$, and its horizontal divergence, $|\nabla_h \cdot \mathbf{B}_h|$, were statistically significant but much weaker, at 0.14 and 0.28. The lack of correlation with the curl suggests that electric current densities do not play a strong role in Ca II emission. We also found a significant correlation, 0.42, between Ca II and filling factor in the subset of pixels in which filling factors were estimated.

For the Poynting flux, the correlation of Ca II intensity with unsigned and signed f -weighted Poynting fluxes was 0.53, and 0.19, respectively. The fact that the magnetic variables that enter the Poynting flux are more strongly correlated with Ca II emission than the Poynting flux suggests that the only additional information in the Poynting flux, from the FLCT flows, is unrelated to Ca II emission; and, indeed, the correlation of Ca II with $|\mathbf{v}_h|$ is significantly negative, at -0.11. This anticorrelation probably arises because flow speeds are higher in weak-field regions, while the emission is brightest in strong-field regions. Correlations with the horizontal curl of \mathbf{v}_h , $|\hat{\mathbf{z}} \cdot (\nabla_h \times \mathbf{v}_h)|$, and its horizontal divergence, $|\nabla_h \cdot \mathbf{v}_h|$, were also negative, but marginally insignificant at -0.07 and -0.08, respectively. We also checked the *signed* horizontal flow divergence, reasoning that converging flows might slightly compress the plasma and lead to heating. The correlation was also negative (i.e., converging motions are present slightly more often near brighter Ca II emission), and stronger but still weak, at -0.12. This might be related to the concentration of magnetic flux in downflow lanes where horizontal flows converge. The weak correlation with the curl here implies that resolved braiding / vortical motions

(e.g., Parker 1983, Kitiashvili et al. 2014) do not play a strong role in the generation of Ca II emission. The reason why the correlation with the curl is negative is hard to understand, but might be related to the presence of stronger flows in weaker-field regions.

This analysis suggests that flow information at the spatial and temporal scales that we study has relatively little bearing on Ca II emission, compared to magnetic variables. Tarbell (private communication) notes that Ca II images from SOT like that which we analyzed here are “mostly photospheric” due to the relatively wide wavelength band, and suggests that enhanced emission in areas with strong photospheric fields arises from the hot-wall effect (Topka et al. 1997), not chromospheric heating.

4. Summary & Conclusions

By combining LCT velocities estimated from a LOS magnetogram sequence with a vector magnetogram, both derived from *Hinode*/SOT observations of AR 10930, we estimated the Poynting flux, under the frozen-in-flux assumption, in a (12 Mm \times 12 Mm) plage region to be $4.9 - 5.5 \times 10^7$ erg cm $^{-2}$ s $^{-1}$, depending upon whether FLCT or SLCT velocities were used. Errors in the magnetic fields likely produce smaller uncertainties in the Poynting flux than this. These Poynting fluxes are greater than the chromospheric and coronal energy demands estimated by Withbroe & Noyes (1977), $\sim 2 \times 10^7$ erg cm $^{-2}$ s $^{-1}$ and $\sim 1 \times 10^7$ erg cm $^{-2}$ s $^{-1}$, respectively.

We found that the Poynting flux varied in sign across the plage region that we studied. By plotting the distribution of Poynting fluxes in this region’s pixels, we found that the mean upward flux arose from a predominance of upward-flux pixels toward the high-Poynting-flux end of the distribution. We then identified “plage-like” pixels — those with nearly vertical flux densities in the range 100 – 1500 Mx cm $^{-2}$, and sufficient polarization for the vector field to be estimated — across the rest of the active region. The distribution of Poynting fluxes in this set of plage-like pixels exhibited the same systematic prevalence of upward-flux pixels, suggesting that the plage region that is the focus of our study is not a special case.

In analogy with the study by Fisher et al. (1998) relating active regions’ soft X-ray luminosities to magnetic field properties, we investigated correlations of Poynting fluxes with properties of the magnetic and velocity fields. We found that both the *unsigned* and *signed* Poynting fluxes typically increase with pixels’ field strengths. Correlations of Poynting fluxes with both unsigned vertical electric current density and flow vorticity were relatively weak, suggesting braiding or vortical motions (e.g., Parker 1983, Kitiashvili et al. 2014) are not key aspects of the energy transport process. Building upon the work of Fisher et al. (1998), Pevtsov et al. (2003) found that soft X-ray luminosities for a range of magnetic regions on the Sun scaled nearly linearly with flux, with a relationship approximating $\sim 10^3$ erg s $^{-1}$ Mx $^{-1}$. Here, we found the energy input per unit magnetic flux to be on the order of 10^5 erg s $^{-1}$ Mx $^{-1}$. We found that fields with intrinsic vertical field strengths of ~ 1300 G supply the bulk of the

net Poynting flux.

We also compared our Poynting flux map with a Ca II intensity image, and found much stronger correlation of Ca II emission with the vertical magnetic field strength $|B_z|$ than with vertical Poynting flux. We noted that this magnetic correlation might, however, arise from near-photospheric emission in the passband exhibiting the hot-wall effect in strong fields.

The time interval Δt between images (eight minutes here) and windowing length scale L (4 pixels, ~ 1 Mm) used in our tracking will likely filter out processes on shorter temporal and spatial scales. Such processes (e.g., waves, or smaller-scale braiding) might play key roles in chromospheric emission. Given that chromospheric and coronal length scales are shorter than the scales we resolve, observations with higher resolution in space and time (see below) would be useful to investigate Poynting flux – emission correlations further. It should be noted, however, that our energy flux is large enough that sub-resolution dynamics are not required to explain the observed coronal heating.

This initial study leaves several questions unanswered, motivating related studies to extend the work here. Do other tracking methods yield similar results? The same plage region analyzed here could be tracked with other methods (e.g., DAVE or DAVE4VM; Schuck 2006, Schuck 2008) to better understand the model-dependence of flow estimates in determining Poynting fluxes. How are photospheric Poynting fluxes related to emission from the overlying atmosphere? To address this question, it would be useful to analyze additional *Hinode*/SOT datasets, especially observations with simultaneous IRIS (De Pontieu et al. 2014) coverage of chromospheric, transition region, and coronal emission, to seek any evidence of spatial or temporal correlations between energy input via our estimated Poynting fluxes and energy dissipation in the outer solar atmosphere. How rapidly does the spatial distribution of the Poynting flux vary in time? In contrast to the snapshot we analyze here, successive Poynting flux maps would be needed to address this question. While SP vector magnetograms are the best currently available, the telemetry limitations of *Hinode* preclude long-duration runs of successive, rapid rasters over moderately large FOVs. Consequently, the HMI instrument aboard SDO (Scherrer et al. 2012) could be used investigate the temporal variation of the Poynting flux. Unfortunately, HMI has both worse spatial resolution and poorer spectral sampling. So a related question is: How sensitively do estimates of the Poynting flux depend upon a magnetograph’s spatial and spectral resolution? Analysis of a region simultaneously observed with SOT and HMI would be worthwhile. (It is probable, in fact, that additional energy flux could be resolved with even higher-resolution observations, though the energy flux must begin to decrease at some limit, to avoid an ultraviolet catastrophe. This motivates studies with new, higher-resolution instruments, as discussed below.)

Within the larger context of the coronal heating problem, we suggest that a key strategic observational objective for understanding chromospheric and coronal heating should be construction of a detailed energy budget for the photosphere-to-corona system, with spatially

and temporally resolved energy inputs correlated with energy release in all forms — radiation, kinetic energy in thermal and non-thermal particles and bulk motion, and gravitational potential energy. This will require high-resolution and high-cadence observations of the magnetic field and emission throughout the photosphere-to-corona system, for which both space-based observatories (e.g., SDO, IRIS, and the planned Solar-C satellite¹) and existing and planned ground-based observatories (NST [Goode et al.2010], GREGOR [Volkmer et al. 2010], ATST [Rimmele et al. 2010], and EST [Zuccarello and Zuccarello 2011]) will be essential.

Acknowledgments: We thank the *Hinode* science teams for their hard work in producing the excellent data that made this study possible. We thank: the referee for constructive criticisms that we believe improved the manuscript; Anthony Yeates for pursuing estimation of the Poynting flux in unipolar regions, which inspired this work; NWRA’s K. D. Leka for help with SP data prepared by the late Tom Metcalf; Bruce Lites for providing error estimates from the ASP inversions of the SP data and suggestions regarding interpretation of the data; and T.D. Tarbell and G.H. Fisher for providing useful comments about the manuscript that helped improve it. B.T.W. also gratefully thanks the Japan Society for the Promotion of Science, whose fellowship supported much of the work that underlies this study, and acknowledges funding from the NSF’s National Space Weather Program under award AGS-1024862, the NASA Living-With-a-Star TR&T Program (grant NNX11AQ56G), and the NASA Heliophysics Theory Program (grant NNX11AJ65G). The authors are grateful to Japanese and U.S. taxpayers for providing the funds necessary to perform this work. *Hinode* is a Japanese mission developed and launched by ISAS/JAXA, collaborating with NAOJ as a domestic partner, and NASA and STFC (UK) as international partners. Scientific operation of the *Hinode* mission is conducted by the *Hinode* science team organized at ISAS/JAXA. This team mainly consists of scientists from institutes in the partner countries. Support for the post-launch operation is provided by JAXA and NAOJ (Japan), STFC (UK), NASA (USA), ESA, and NSC (Norway).

References

- Bercik, D. J. 2002, PhD thesis, Michigan State University
Berger, T. E., Loefeldahl, M. G., Shine, R. S., & Title, A. M. 1998, ApJ, 495, 973
Bingert, S. & Peter, H. 2011, A&A, 530, A112
Brown, D. S., Nightingale, R. W., Alexander, D., Schrijver, C. J., Metcalf, T. R., Shine, R. A., Title, A. M., & Wolfson, C. J. 2003, Sol. Phys., 216, 79
Close, R. M., Parnell, C. E., Longcope, D. W., & Priest, E. R. 2004, ApJL, 612, L81
Démoulin, P. & Berger, M. A. 2003, Sol. Phys., 215, 203
De Pontieu, B., Title, A. M., Lemen, J., Kushner, G. D., Akin, D. J., Allard, B., Berger, T., Boerner, P., Cheung, M., Chou, C., Drake, J. F., Duncan, D. W., Freeland, S., Heyman, G. F., Hoffman, C., Hurlburt, N. E., Lindgren, R. W., Mathur, D., Rehse, R., Sabolish, D., Seguin, R., Schrijver,

¹ http://hinode.nao.ac.jp/SOLAR-C/Documents/Solar-C_e.pdf

- C. J., Tarbell, T. D., Wuelser, J.-P., Wolfson, C. J., Yanari, C., Mudge, J., Nguyen-Phuc, N., Timmons, R., van Bezooijen, R., Weingrod, I., Brookner, R., Butcher, G., Dougherty, B., Eder, J., Knagenhjelm, V., Larsen, S., Mansir, D., Phan, L., Boyle, P., Cheimets, P. N., DeLuca, E. E., Golub, L., Gates, R., Hertz, E., McKillop, S., Park, S., Perry, T., Podgorski, W. A., Reeves, K., Saar, S., Testa, P., Tian, H., Weber, M., Dunn, C., Eccles, S., Jaeggli, S. A., Kankelborg, C. C., Mashburn, K., Pust, N., Springer, L., Carvalho, R., Kleint, L., Marmie, J., Mazmanian, E., Pereira, T. M. D., Sawyer, S., Strong, J., Worden, S. P., Carlsson, M., Hansteen, V. H., Leenaarts, J., Wiesmann, M., Aloise, J., Chu, K.-C., Bush, R. I., Scherrer, P. H., Brekke, P., Martinez-Sykora, J., Lites, B. W., McIntosh, S. W., Uitenbroek, H., Okamoto, T. J., Gummin, M. A., Auken, G., Jerram, P., Pool, P., & Waltham, N. 2014, ArXiv e-prints
- Fisher, G. H., Longcope, D. W., Metcalf, T. R., & Pevtsov, A. A. 1998, *ApJ*, 508, 885
- Fisher, G. H. & Welsch, B. T. 2008, in *Astronomical Society of the Pacific Conference Series*, Vol. 383, *Subsurface and Atmospheric Influences on Solar Activity*, ed. R. Howe, R. W. Komm, K. S. Balasubramaniam, & G. J. D. Petrie, 373–380; also arXiv:0712.4289
- Fludra, A. & Ireland, J. 2008, *A&A*, 483, 609
- Galsgaard, K. & Nordlund, Å. 1996, *J. Geophys. Res.*, 101, 13445
- Golub, L., Maxson, C., Rosner, R., Vaiana, G. S., & Serio, S. 1980, *ApJ*, 238, 343
- Goode, P. R., Coulter, R., Gorceix, N., Yurchyshyn, V., & Cao, W. 2010, *Astronomische Nachrichten*, 331, 620
- Gudiksen, B. V. & Nordlund, Å. 2002, *ApJ*, 572, L113
- Hagenaar, H., Schrijver, C., Title, A., & Shine, R. 1999, *ApJ*, 511, 932
- Hahn, M., Landi, E., & Savin, D. W. 2012, *ApJ*, 753, 36
- Ichimoto, K., Lites, B., Elmore, D., Suematsu, Y., Tsuneta, S., Katsukawa, Y., Shimizu, T., Shine, R., Tarbell, T., Title, A., Kiyohara, J., Shinoda, K., Card, G., Lecinski, A., Ständer, K., Nakagiri, M., Miyashita, M., Noguchi, M., Hoffmann, C., & Cruz, T. 2008, *Sol. Phys.*, 249, 233
- Isobe, H., Kubo, M., Minoshima, T., Ichimoto, K., Katsukawa, Y., Tarbell, T. D., Tsuneta, S., Berger, T. E., Lites, B., Nagata, S., Shimizu, T., Shine, R. A., Suematsu, Y., & Title, A. M. 2007, *PASJ*, 59, 807
- Kano, R., Ueda, K., & Tsuneta, S. 2014, *ApJL*, 782, L32
- Katsukawa, Y. & Tsuneta, S. 2005, *ApJ*, 621, 498
- Kitiashvili, I. N. 2014, ArXiv e-prints
- Klimchuk, J. A. 2006, *Sol. Phys.*, 234, 41
- Kosugi, T., Matsuzaki, K., Sakao, T., Shimizu, T., Sone, Y., Tachikawa, S., Hashimoto, T., Minesugi, K., Ohnishi, A., Yamada, T., Tsuneta, S., Hara, H., Ichimoto, K., Suematsu, Y., Shimojo, M., Watanabe, T., Shimada, S., Davis, J. M., Hill, L. D., Owens, J. K., Title, A. M., Culhane, J. L., Harra, L. K., Doschek, G. A., & Golub, L. 2007, *Sol. Phys.*, 243, 3
- Lites, B. W., Akin, D. L., Card, G., Cruz, T., Duncan, D. W., Edwards, C. G., Elmore, D. F., Hoffmann, C., Katsukawa, Y., Katz, N., Kubo, M., Ichimoto, K., Shimizu, T., Shine, R. A., Ständer, K. V., Suematsu, A., Tarbell, T. D., Title, A. M., & Tsuneta, S. 2013, *Sol. Phys.*, 283, 579
- Liu, Y. & Schuck, P. W. 2012, *ApJ*, 761, 105

- Longcope, D. W. 2004, *ApJ*, 612
- Martínez Pillet, V., Lites, B. W., & Skumanich, A. 1997, *ApJ*, 474, 810
- Meyer, K. A., Sabol, J., Mackay, D. H., & van Ballegooijen, A. A. 2013, *ApJL*, 770, L18
- Moon, Y.-J., Chae, J., Choe, G. S., Wang, H., Park, Y. D., Yun, H. S., Yurchyshyn, V., & Goode, P. R. 2002, *ApJ*, 574, 1066
- November, L. & Simon, G. 1988, *ApJ*, 333, 427
- Parker, E. N. 1983, *ApJ*, 264, 635
- Parker, E. N. 1983, *ApJ*, 264, 642
- Parker, E. N. 1984, *ApJ*, 280, 423
- Parker, E. N. 1988, *ApJ*, 330, 474
- Parnell, C. E. & De Moortel, I. 2012, *Royal Society of London Philosophical Transactions Series A*, 370, 3217
- Pevtsov, A. A., Fisher, G. H., Acton, L. W., Longcope, D. W., Johns-Krull, C. M., Kankelborg, C. C., & Metcalf, T. R. 2003, *ApJ*, 598, 1387
- Press, W. H., Teukolsky, S. A., Vetterling, W. T., & Flannery, B. P. 1992, *Numerical Recipes in C: The art of scientific computing*, Second Edition (Cambridge: Cambridge University Press)
- Rappazzo, A. F., Velli, M., Einaudi, G., & Dahlburg, R. B. 2008, *ApJ*, 677, 1348
- Rimmele, T. R., Wagner, J., Keil, S., Elmore, D., Hubbard, R., Hansen, E., Warner, M., Jeffers, P., Phelps, L., Marshall, H., Goodrich, B., Richards, K., Hegwer, S., Kneale, R., & Ditsler, J. 2010, in *Society of Photo-Optical Instrumentation Engineers (SPIE) Conference Series*, Vol. 7733, *Society of Photo-Optical Instrumentation Engineers (SPIE) Conference Series*
- Scherrer, P. H., Schou, J., Bush, R. I., Kosovichev, A. G., Bogart, R. S., Hoeksema, J. T., Liu, Y., Duvall, T. L., Zhao, J., Title, A. M., Schrijver, C. J., Tarbell, T. D., & Tomczyk, S. 2012, *Sol. Phys.*, 275, 207
- Schrijver, C. J., De Rosa, M. L., Metcalf, T., Barnes, G., Lites, B., Tarbell, T., McTiernan, J., Valori, G., Wiegmann, T., Wheatland, M. S., Amari, T., Aulanier, G., Démoulin, P., Fuhrmann, M., Kusano, K., Régnier, S., & Thalmann, J. K. 2008, *ApJ*, 675, 1637
- Schrijver, C. J., Title, A. M., Harvey, K. L., Sheeley, N. R., Wang, Y.-M., van den Oord, G. H. J., Shine, R. A., Tarbell, T. D., & Hurlburt, N. E. 1998, *Nature*, 394, 152
- Schuck, P. W. 2006, *ApJ*, 646, 1358
- . 2008, *ApJ*, 683, 1134
- Schwadron, N. A., McComas, D. J., & DeForest, C. 2006, *ApJ*, 642, 1173
- Shimizu, T., Nagata, S., Tsuneta, S., Tarbell, T., Edwards, C., Shine, R., Hoffmann, C., Thomas, E., Sour, S., Rehse, R., Ito, O., Kashiwagi, Y., Tabata, M., Kodeki, K., Nagase, M., Matsuzaki, K., Kobayashi, K., Ichimoto, K., & Suematsu, Y. 2008, *Sol. Phys.*, 249, 221
- Suematsu, Y., Tsuneta, S., Ichimoto, K., Shimizu, T., Otsubo, M., Katsukawa, Y., Nakagiri, M., Noguchi, M., Tamura, T., Kato, Y., Hara, H., Kubo, M., Mikami, I., Saito, H., Matsushita, T., Kawaguchi, N., Nakaoji, T., Nagae, K., Shimada, S., Takeyama, N., & Yamamuro, T. 2008, *Sol. Phys.*, 249, 197
- Tan, C., Jing, J., Abramenko, V. I., Pevtsov, A. A., Song, H., Park, S.-H., & Wang, H. 2007, *ApJ*, 665, 1460

- Title, A. M., Topka, K. P., Tarbell, T. D., Schmidt, W., Balke, C., & Scharmer, G. 1992, *ApJ*, 393, 782
- Tomczyk, S., McIntosh, S. W., Keil, S. L., Judge, P. G., Schad, T., Seeley, D. H., & Edmondson, J. 2007, *Science*, 317, 1192
- Topka, K. P., Tarbell, T. D., & Title, A. M. 1997, *ApJ*, 484, 479
- Tsuneta, S., Ichimoto, K., Katsukawa, Y., Nagata, S., Otsubo, M., Shimizu, T., Suematsu, Y., Nakagiri, M., Noguchi, M., Tarbell, T., Title, A., Shine, R., Rosenberg, W., Hoffmann, C., Jurcevic, B., Kushner, G., Levay, M., Lites, B., Elmore, D., Matsushita, T., Kawaguchi, N., Saito, H., Mikami, I., Hill, L. D., & Owens, J. K. 2008, *Sol. Phys.*, 249, 167
- Volkmer, R., von der Lühe, O., Denker, C., Solanki, S. K., Balthasar, H., Berkefeld, T., Caligari, P., Collados, M., Fischer, A., Halbgewachs, C., Heidecke, F., Hofmann, A., Klvaňa, M., Kneer, F., Lagg, A., Popow, E., Schmidt, D., Schmidt, W., Sobotka, M., Soltau, D., & Strassmeier, K. G. 2010, *Astronomische Nachrichten*, 331, 624
- Welsch, B. T., Abbett, W. P., DeRosa, M. L., Fisher, G. H., Georgoulis, M. K., Kusano, K., Longcope, D. W., Ravindra, B., & Schuck, P. W. 2007, *ApJ*, 670, 1434
- Welsch, B. T., Fisher, G. H., & Sun, X. 2013, *ApJ*, 765, 98
- Welsch, B. T., Kusano, K., Yamamoto, T. T., & Muglach, K. 2012, *ApJ*, 747, 130
- Welsch, B. T., Li, Y., Schuck, P. W., & Fisher, G. H. 2009, *ApJ*, 705, 821
- Withbroe, G. L. & Noyes, R. W. 1977, *ARA&A*, 15, 363
- Yeates, A. R., Bianchi, F., Welsch, B. T., & Bushby, P. J. 2014, *A&A*, 564, A131
- Zuccarello, F. & Zuccarello. 2011, in *IAU Symposium*, Vol. 274, *IAU Symposium*, ed. A. Bonanno, E. de Gouveia Dal Pino, & A. G. Kosovichev, 310–313